

Electromagnetic Field
Measurements inside Photonic
Crystals developing a Photonic Free
Electron Laser

Universiteit Twente and Saxion Hogescholen

Bachelor's thesis from

Bob Reijnders

June 2011

Contents

1	Introduction	1
2	Photonic Free Electron Lasers	3
2.1	Introduction to FELs and pFELs	3
2.2	Cherenkov Radiation	5
2.3	Bunching Principle	10
3	PhC and Waveguiding Principles	13
3.1	Introduction	13
3.2	Wave motion	13
3.3	TM modes in metallic rectangular waveguides	14
3.4	Wave propagation in a PhC	19
3.5	Field distribution measurement	21
4	Experimental results	25
4.1	Introduction	25
4.2	Measurement of band structure	25
4.3	Field Characterization	29
5	Conclusion	33
5.1	Recommendations	34
A	Phase and Group velocity of light	35
A.1	Modulated Wave	35
A.2	Phase and group velocity relation	36
B	Measured and Calculated resonance peaks	39
C	FFT Smoothing	41
	Bibliography	43

List of Figures

2.1	pFEL scheme	4
2.2	Overview	5
2.3	Cherenkov wavefront	6
2.4	Cherenkov wavefront geometry	7
2.5	Dispersion in glass medium	8
2.6	Induced dipoles in a PhC	9
2.7	Dispersion characteristic of a rectangular waveguide	10
2.8	Bunching process	11
2.9	Transverse modes of an E_z -field	12
3.1	Modes in a 1D cavity	14
3.2	Photonic crystal slab	19
3.3	Calculated bandstructure	20
3.4	Calculated cross sections of the transverse E_z -mode patterns for mode 1 and mode 2 of the PhC at $z = 0.5a_z$ (upper fig.) and $z = 2.5a_z$ (lower) fig.	21
4.1	Dispersion measurement schematic	26
4.2	Resonator layout	27
4.3	Transmission Readings	28
4.4	Calculated transmission	29
4.5	Comparison of measured and calculated band structure in the first spatial harmonic	30
4.6	Schematic representation of a Field Characterization setup	30
4.7	Frequency shifts for Transverse Mode 1	31
A.1	Propagation of a modulated wave	36
C.1	Peak frequency detection variation in 2 consecutive PhC dis- persion measurements	41

Chapter 1

Introduction

Photonic crystals (PhC) are periodic dielectric or metallo-dielectric structures engineered to manipulate the properties of light. Photonic crystals can be designed to e.g. slowing down light to extremely low values[1], bend light through sharp corners [2] or prevent certain frequencies light of any polarization from propagating in one or more directions [3]. PhC are therefore proposed for many applications like optical fibers [4], optical computers [5], electron accelerators [6] and free-electron lasers [7, 8] (FEL).

Investigating of the behavior of a PhC usually requires measuring the transmission and reflection spectra. It is possible to derive the band structure from these measurements and hence characterize the PhC. However, as only fields outside the PhC structure are measured, no information is available about the internal field. Numerous applications would benefit from a precise knowledge about this internal field.

Surface near field optical scanning microscopy[9] is often used to measure the optical very close to the surface of the PhC. Although this still measures the field outside the structure, some information can be obtained from the internal field near the surface. Another method uses monopole antennas that are inserted at discrete positions into the PhC along one of the propagation directions of the light[10]. These can then be used to probe propagating and evanescent modes. Although this method allows one to probe the fields deeper inside the PhC, the depth is still limited as the antennas will otherwise significantly disturb the field it measures.

This thesis focusses on a measurement method that allows all the six components of the electromagnetic field (E_x, E_y, E_z and H_x, H_y, H_z) to be mapped at every accessible position inside a PhC. This technique is well known for characterizing fields inside microwave structures[11, 12]. Surprisingly it has never been used to measure fields inside a PhC. The technique relies on placing the PhC inside a resonator and measure the resonance frequencies. If one inserts a sub-wavelength object inside the PhC, the resonant frequencies slightly shift depending on the local field, shape, size and ma-

terial (susceptibility and permeability) of the object. Thus by choosing an appropriate shape, material and orientation each particular field component can be mapped by varying the position of the sub-wavelength object in the PhC.

Here we apply the technique in a PhC designed for a photonic free electron laser (pFEL) under development at the Laser Physics and Nonlinear Optics group from the University of Twente. pFELs are developed to provide a compact, powerful and tunable THz source [8]. Inside a pFEL a continuous stream of electrons pass through a PhC. By the interaction of the electrons with the electric fields inside the crystal the electron beam gets bunched. The bunched electron beam then emits coherent laser light.

The electric field inside the PhC is crucial to the operation of pFEL. Due to inevitable limitations of the manufacturing accuracy an experimental PhC will possess disorder. To investigate the disorders influence on the electric field the PhC properties inside the PhC need to be measured.

The remainder of this thesis is organized as follows. In the first chapter, the pFEL is briefly discussed to provide the requirements for the PhC. The second chapter elaborates on the theoretical basics of waveguiding structures and presents the PhC in more detail. We then continue with the measurement setup used to characterize the PhC. The structure has been characterized in two ways, first the band structure has been measured and second the internal field has been determined. Both type of measurements are compared to numerical calculations using a FDTD field solver. We conclude with a discussion of the results and recommendation for future work.

Chapter 2

Photonic Free Electron Lasers

2.1 Introduction to FELs and pFELs

Free-electron lasers (FEL) are very different to photonic free-electron lasers (pFEL). FELs are devices that use an alternating static magnetic field to convert kinetic energy of relativistic electrons into coherent radiation energy. These devices have the extremely useful property that the wavelength generated depends on the velocity of the electrons. FELs can therefore fill the gaps in the electromagnetic spectrum where no other coherent light sources exist. Examples are the THz gap (FELIX¹, FLARE²) and in the soft- and hard X-ray regime (FLASH, LCLS, FERMI@Elettra). However, the scaling is such that shorter wavelengths require higher electron energies, e.g., a few tens MeV for a THz source and a few GeV for the soft X-ray wavelengths. Consequently FELs are very big and expensive facilities.

In a photonic free electron laser (pFEL) electrons propagate with velocities much smaller than the speed of light through a photonic crystal (PhC). The electrons emit radiation inside the PhC through the Cherenkov effect. Cherenkov radiation is emitted whenever charge particles move faster than phase velocity³ of the radiation. Therefore, Cherenkov radiation is only emitted when the particles move through a medium, as in a vacuum the radiation always moves faster than the electrons. When the medium is a photonic crystal (PhC), one can take full advantage of the PhC to engineer the propagation of the light. For example, the light can be slowed down considerably [1] and this allows the use of low energy electrons i.e. the velocity of electrons is a small fraction of the speed of light in vacuum. Before discussing the two main physics principles behind the pFEL we will first

¹Part of GUTHz research at FOM Institute for Plasma Physics Rijnhuizen

²Build at the Radboud University Nijmegen

³See Appendix A at pag. 35 for a small review on phase velocities

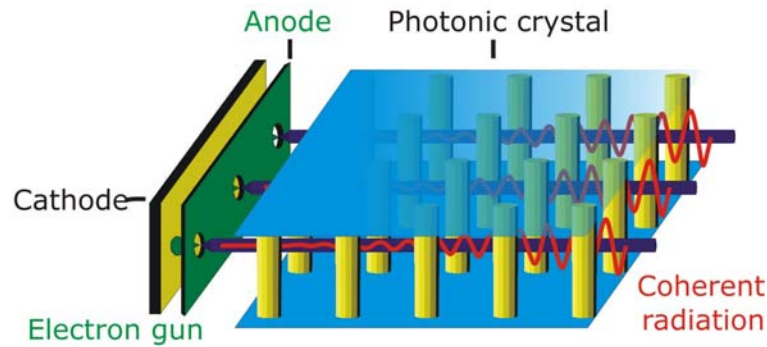


Figure 2.1: pFEL scheme

briefly present an overview of the device.

Fig. 2.1 shows the schematical overview of a pFEL. The electrons are produced in the electron gun shown on the left in fig. 2.1. The electron gun produces one or multiple low energy electrons beams that stream through the PhC, shown in the fig. on the right. Depending on the size and number of electron beams, thermionic emission or field emission can be used. The latter is shown schematically in fig. 2.1).

The pFEL at LPNO however initially uses a single beam produced by a *thermionic electron gun*. Here the cathode surface is heated, so that only a small energy is required to overcome the surface binding force i.e., work function⁴. The external applied voltage between cathode and anode is now sufficient to extract the electrons and accelerate them from cathode to anode. Efficient operation requires a low work function and thus the device needs to be operated under a vacuum of 10^{-8} mbar. The electron gun nominally operates at 15-20 kV, i.e., electrons stream at approx. 0.3 times c , where c is the speed of light in vacuum.

Alternatively, when a large number of separate electron beams are required, a *field emission cathode* can be used (see fig. 2.1). Here the cathode consists of regular array of cones with very sharp tips placed in front of small holes in the extraction electrode. A small voltage between the cathode and anode creates a high field at the tip due to field enhancement. This high field extracts the electrons from the tip which are subsequently accelerated towards the anode. This type of cathode allows for a regular array of finely spaced electron beams.

In both cases an external guiding field must be provided to prevent electron beam divergence in the PhC caused by Coulomb repulsion. Here a solenoid is used (see fig. 2.2) as this magnetic field converts the radial

⁴In solid state physics, the work function is the minimum energy (usually presented in electron volts) needed to remove an electron from a solid to a point immediately outside the solid surface.

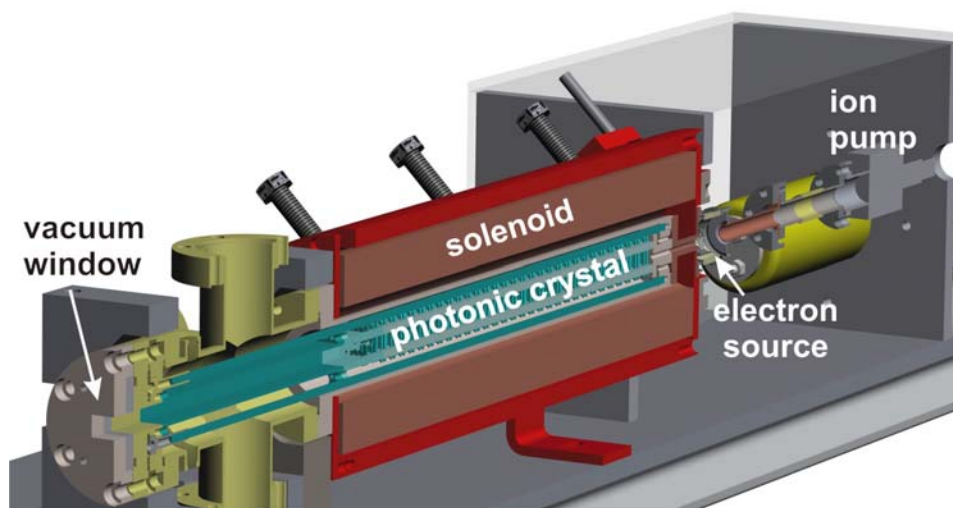


Figure 2.2: Overview

expansion in a circular motion around the axis of propagation. Behind the PhC, at the vacuum window in fig. 2.2, the radiation is coupled out of the device.

The PhC has two functions. First it slows down the phase velocity of the electrons so that Cherenkov emission is possible. Second, the electron beam gets bunched by the scattering of the light emitted from the individual electrons at the periodic structure, eventually leading to coherent emission. Both processes will be described in more detail in the following sections.

2.2 Cherenkov Radiation

The electron interaction with the photonic crystals is based on the Cherenkov radiation principle. Cherenkov radiation was first characterized by Pavel Alekseyevich Cherenkov (1904–1990) who shared the Nobel prize in Physics in 1958 for his work on this subject. The radiation is well known from nuclear facilities where high velocity charged particles travel through the cooling water. The charged particles, mostly electrons, produce light creating a glow around radioactive materials.

Electrons carry a negative charge. When an electron comes along a water molecule of the cooling water, it polarizes the water molecule. When the electron has passed the molecule depolarizes again. This process induces an oscillating dipole. During the dampening out dipole radiation is emitted from the water molecule. Constructive interference of all the emissions induced by a single electron occur only when the phase velocity of light in the surrounding medium v_{ph} is less or equal to the speed of the electron v_e .

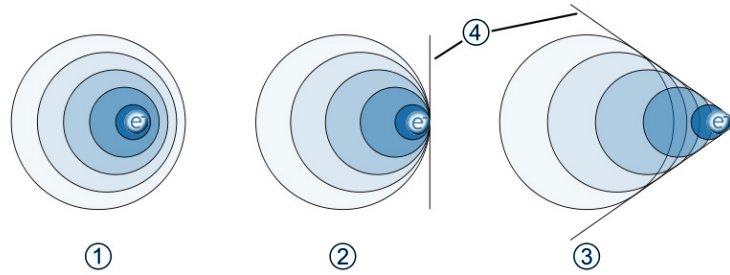


Figure 2.3: Cherenkov wavefront

Fig. 2.3 illustrates this by showing the emission process for electrons being slower, faster or having the same velocity as the phase velocity in water. The blue beads marked 'e' depict an electron (or any other charged particle) traveling towards the right. Each circle is a spherical elementary wavelet due to the dipole emission. The wavelet is generated by a water molecule in the center of that circle and expands in all directions over time with a phase velocity v_{ph} . Thus a larger circle radius means an earlier emission. Black lines, denoted by the number 4, are Cherenkov wavefronts which constructively interfere. These wavefronts form the radiation which are observed in nuclear plants.

Illustration 1 in fig. 2.3, shows an electron with $v_e < v_{ph}$ having passed 5 water molecules, i.e. 5 molecules emitted radiation earlier. The radiation travels faster than the electron. Therefore new wavelets are always trailing behind older ones and no constructive interference occurs between successively emitted waves. Thus if the $v_e < v_{ph}$ no constructive interference occurs and no net light emission is observed. The electron velocity stays unchanged.

Illustration 2 in fig. 2.3, shows an electron moving at exactly the speed of the emitted dipole radiation $v_e = v_{ph}$. The overlapping circles show that each emitted wavelet constructively interferes just in front of the electron. Therefore a wavefront along the vertical line marked by number 4 forms and light is observed. The electrons slow down a little bit.

When v_e is even higher, e.g. the electron traveling over twice the speed of light in the medium $v_e > v_{ph}$, a cone is formed, see illustration 3 in fig. 2.3. Along the cone the individual wavelets are in phase with each other. This wavefront has an angle θ to the normal of propagation. To calculate the angle θ we draw a triangle as in fig. 2.4. The left corner of the triangle represents the initial location of the electron. After a time t the electron is at the right corner. The electron has traveled a distance $L_e = v_e t$ while the wavefront has traveled $L_{ph} = v_{ph} t$. Taking the cosine of the left angle results in the time independent solution

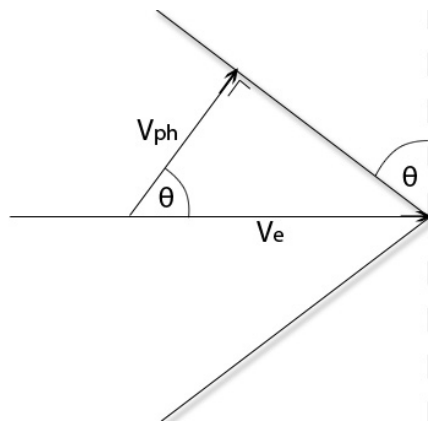


Figure 2.4: Cherenkov wavefront geometry

$$\cos\theta = \frac{v_{ph}}{v_e} \quad (2.1)$$

The shown emission occurs only for $v_e \geq v_{ph}$. When $v_e = v_{ph}$ the angle θ is 0 resulting in a flat wavefront normal to the direction of propagation. As the velocity of the electron increases, so does the angle θ . Note that for every electron velocity higher than the phase velocity an angle θ exists between 0 and 90 degrees.

Relativity theory states that the speed of light c in vacuum is a constant, meaning the Cherenkov emission does not occur in vacuum as electrons cannot be accelerated above c . The lights phase velocity in a dielectric is reciprocal to the refractive index of the medium[13], eq. 2.2:

$$v_{ph} = \frac{c}{n} \quad (2.2)$$

Here v_{ph} is the lights phase velocity, n the refractive index of the medium and c the speed of light in vacuum. For example, water has a refractive index of $n \approx 1.33$ for the visible light. The speed of light in water then is $c/1.33 = 0.75c$. Thus a charged particle propagating with relativistic velocity is then much faster than the speed of light, leading to Cherenkov emission.

The refractive index n is either a constant or varies with the light's frequency, depending on the material. The phenomenon where the refractive index is frequency dependant is called *dispersion*. Dispersion can be caused by material properties or by geometric properties. An example for dispersion is the working of a prism. The dispersion of the glass causes different colors

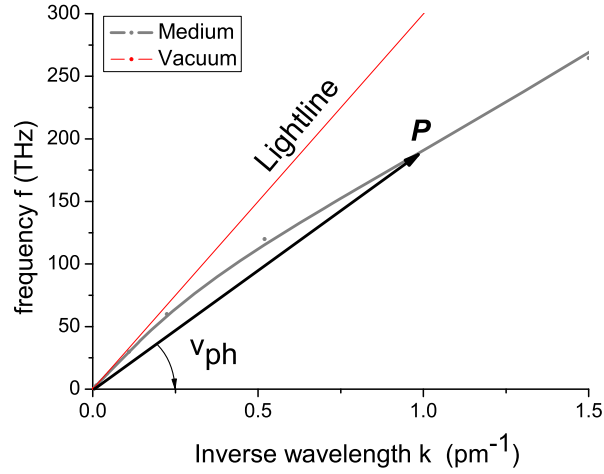


Figure 2.5: Dispersion in glass medium

of light to refract at different angles, splitting white light into a rainbow of colors.

Fig: 2.5 shows a dispersion diagram where the angular frequency of the incident light ω is plotted against the wavenumber k . The black line is the dispersion of glass. The red graph red line shows the dispersion of vacuum. This line is also named lightline. The general expression of dispersion[13] is given by eq. 2.3

$$v_{ph} = \frac{c}{n(\omega)} = \frac{\omega}{k} \quad (2.3)$$

The phase velocity of light can be read from the dispersion diagram when the wave number is known. The slope of a line, pointing out from the origin towards the dispersion diagram is the phase velocity. This makes clear why the red line of fig: 2.5 is called the lightline. The graph starts at the origin and its slope is exactly c . Thus all points on this line have phase velocities equal to the light velocity in vacuum. Points below the lightline denote velocities less than c and above the line greater than c .

The equivalents of water molecules in the coolingwater are metal posts of the investigated PhC. Inside a metal the electric field must be 0. Metals shift surface charges to counteract infringing electric fields. In fig: 2.6 the response of metal posts due to a passing electron is shown. The metal posts are depicted in yellow, the electron in blue. All dipoles point toward the passing charge. When the electron has passed along the metal posts they depolarize to their neutral states. Just like the water molecules a short

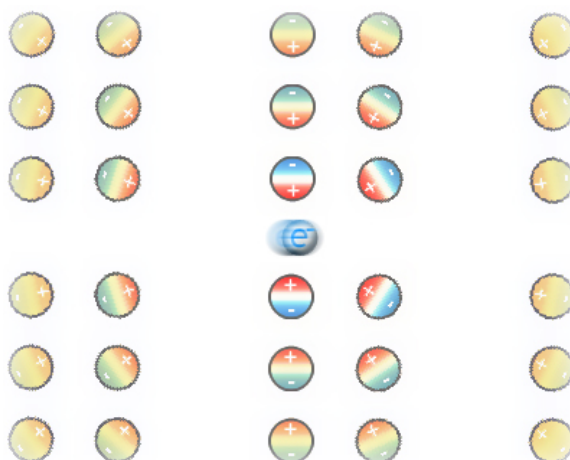


Figure 2.6: Induced dipoles in a PhC

wavelet is generated[14] when this happens. A single electron generates a single wavelet at each post it passes.

To reduce divergence losses the PhC is embedded in a rectangular waveguide. Waveguides cause dispersion change due to their geometry. A dispersion graph of a rectangular waveguide is shown in fig: 2.7(a). The red graph is the lightline, the grey graph the dispersion characteristic of the rectangular waveguide. Note that the graph always lies above the lightline. The phase velocity is higher than the speed of light. An electron can never reach such velocities and no Cherenkov emission occurs in a rectangular waveguide.

However, the metal posts of the PhC induce an artificial increase of the refractive index. Each wavelet is reflected between the metal posts a great number of times along a complex path, slowing the effective propagation velocity of the wavelet down. In fig: 2.7(b) an example of the dispersion characteristic of a fictitious PhC loaded rectangular waveguide is shown. The dashed red line is the lightline and again the gray line the rectangular waveguide dispersion. The green line is the dispersion graph of a PhC waveguide. The blue line is an isovelocity line indicating $0.67c$, or two thirds lightspeed. With increasing k the phase velocity inside a PhC slows down. From about 5 inverse meters and up, the phase velocity inside the example is slower than the speed of light in vacuum. In this region the Cherenkov condition is fulfilled and emission occurs.

The possible emission frequencies are determined by the electron velocity. The velocity is plotted in the dispersion diagram. If e.g. electrons were to travel at $0.67c$, the electron velocity would be equal to the velocity indicated by the blue line in fig. 2.7(b). The point where the electron velocity line and the dispersion graph intersect, indicated by the arrow, determines the

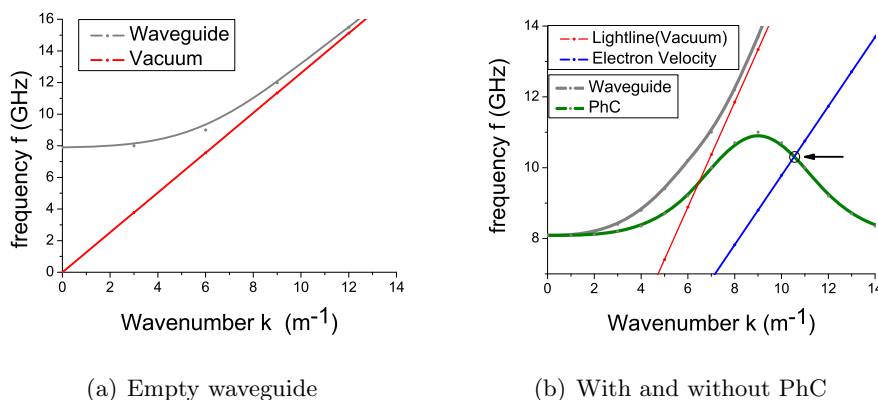


Figure 2.7: Dispersion characteristic of a rectangular waveguide

frequency emitted due to the Cherenkov effect. The emissions are incoherent unless bunching is achieved.

2.3 Bunching Principle

Initially the electron beam is continuous in time. Thus Cherenkov wave fronts are generated at any time t and the wavelets emitted by different electrons have a random phase relation. This means only incoherent radiation is produced. To achieve coherent radiation phases must be aligned through a spatial structuring of the electron beam named bunching.

Assume a co-propagating radiation field with non-zero E_z component along the axis of propagation, z , of the electrons. For a co-propagating E_z -field the phase velocity is $v_{ph} = v_e$ which is the lower limit for Cherenkov emission. Generally the E_z -field will have a periodicity in z , e.g. a sine-like function $\Psi(z)$ with a corresponding potential $\nabla\psi(z) = \Psi(z)$ Fig. 2.8 schematically shows how the potential $\psi(z)$ leads to electron bunching.

First electrons - both blue and green dots - are continuously distributed over the potential which is drawn in red. Due to the potential the electrons are forced into regions of lower potential which is indicated by the blue arrows in 2.8(b).

After some propagation distance Z_1 all electrons get bunched at the potential minimum, see fig. 2.8(c). Each electron in a bunch induces Cherenkov emission with the same phase as the other electrons in the same bunch. Note, in the special case where $v_{ph} = v_e$, the bunches are formed at the minimum of the field potential and since the potential minima of the E_z -field are one wavelength apart, the bunches are also formed one wavelength apart. The emitted waves from individual bunches constructively interfere with each

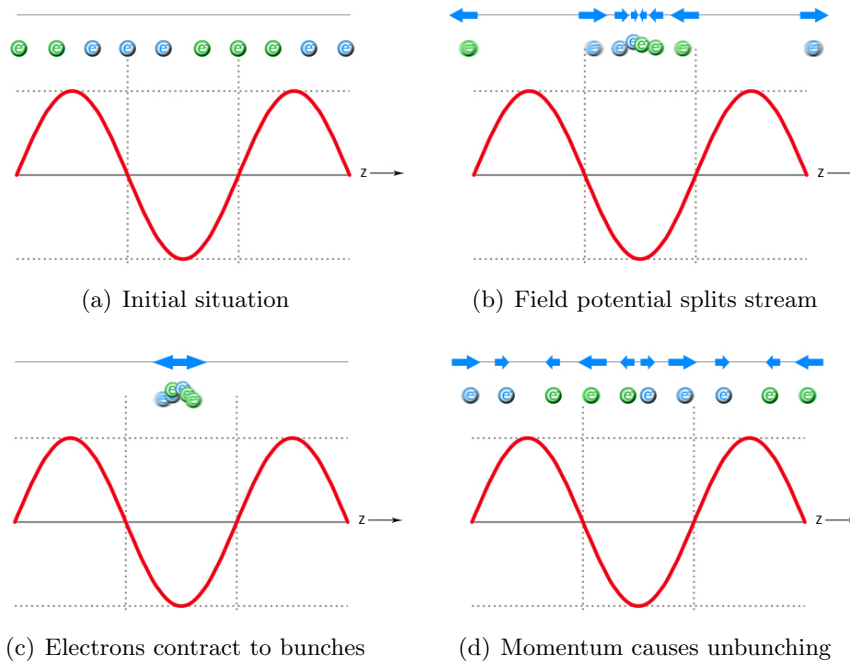


Figure 2.8: Bunching process

other and also with all the waves from other bunches. Thereby coherent light emission is achieved.

At the bottom of the potential, electrons experience no force by the field. However the electrons still carry momentum at this location due to previous acceleration/deceleration. This leads again to unbunching as depicted in fig. 2.8(d). When space charge forces between individual electrons are neglected this leads to a pendulum motion. Like in the pendulum a continuous exchange between potential energy (field) and kinetic energy occurs. Thus in this small signal gain regime⁵ the pFEL should end after Z_1 .

So far E_z -field has been assumed to exist. In an actual pFEL the first E_z -field is generated by spontaneous Cherenkov emission. To ensure actual gain of the E_z -field, electrons have to be a little faster than the phase velocity of the radiation field. Due to Newton's third law of motion, the field not only exerts force onto the electrons, the electrons exert equal force onto the field. In the case $v_e = v_{ph}$, there are as many electrons accelerated as decelerated by the field meaning no gain of the lightfield occurs. If electrons are launched at just above the phase velocity of the field $v_e > v_{ph}$, the E_z -field decelerates more electrons than it accelerates and kinetic energy of the electrons is transferred to the E_z -field resulting in signal gain.

Obviously an electric field with a strong z -component along the path the

⁵The small-signal gain of a laser medium is the gain obtained for an input signal which is not strong enough not to cause gain saturation.

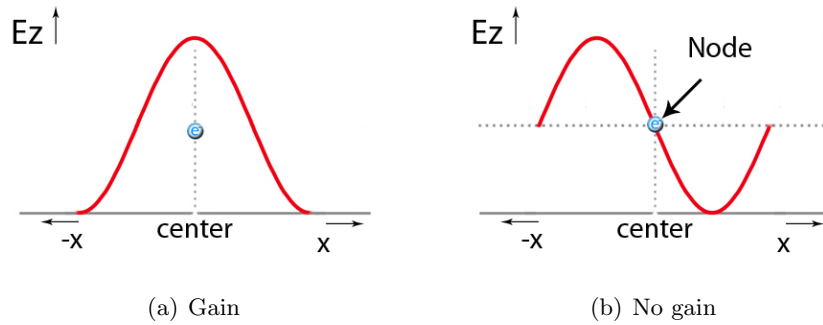


Figure 2.9: Transverse modes of an E_z -field

electrons travel is paramount to the bunching process and signal gain. For high gain the electric field should thus have a maximum at the location of the electron beam.

Furthermore, waveguides and PhC allow many modes of operation. Some of these modes have strong maxima in the center of the PhC, others have nodes. Fig. 2.9 shows two possible transverse mode patterns of the E_z -field. The red line plots the transverse field pattern of the E -field at a fixed position taken along the width-axis x of the PhC. A blue electron is drawn to denote x -position of the electron beam. As seen in fig. 2.9(a), the electron beam in the spFEL propagates exactly at the maximum of the mode-pattern. This allows strong interaction and gain. In fig. 2.9(b) the mode-pattern has a node exactly at the beam path. Electrons have a very weak interaction and generate no gain.

Deviations in the PhC due to manufacturing can deteriorate the field leading to reduced gain, making the measuring of the field inevitably necessary. The next chapter introduces the theory of wave propagation in PhC waveguides.

Chapter 3

PhC and Waveguiding Principles

3.1 Introduction

The operation of a pFEL relies on a slow phase velocity and a strong z component of the electric field of the PhC waveguide. Both properties are determined by the waveguide and embedded PhC geometry. Starting from the waveguide analysis we will show the electric field solutions and dispersion of the PhC waveguide used in the LPNO-UT pFEL experiments.

3.2 Wave motion

To illustrate the waveguide and PhC properties we will largely use the concept of modes. To illustrate modes we first discuss a wave on a string which is fixed on both sides, fig. 3.1.

In fig. 3.1 a string is fixated to a rigid wall at both ends. We assume the string has been excited somehow. Fig. 3.1(a) shows the longest possible oscillation that does not decay with time. The string oscillates up and down forming a stationary wave. Such an steady state oscillation is called a mode of the structure. It has 1 maximum at the center of the cavity and nodes at each wall. Meaning a half wavelength λ fits in the cavity. Fig. 3.1(b) shows the second mode. It has 2 maxima and three nodes, including one in the center. For this mode one wavelength fits into the cavity. For subsequent modes more and more half wavelengths fit into the cavity.

The number of oscillations per second determines the frequency of the wave. As discussed in the previous chapter, to each frequency corresponds an wavenumber determined by the dispersion of the system. For this rope, higher frequencies have shorter wavelengths. In this simplified 1D situation changing from one mode to the other results in discrete frequency steps. Intermediate frequencies produce wavelengths which do not fit the cavity.

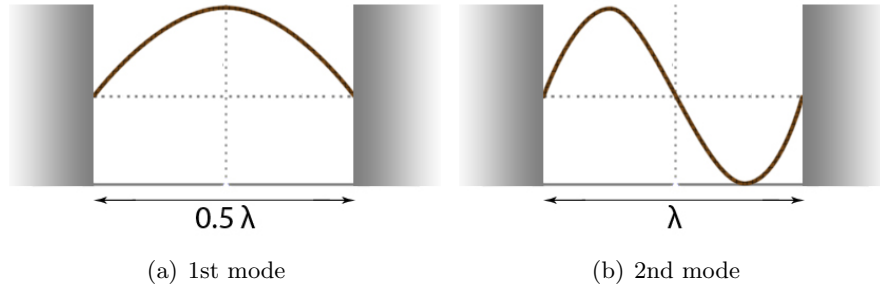


Figure 3.1: Modes in a 1D cavity

These waves will decay exponentially from the point of excitation and thus do not form a mode.

The frequency belonging to the longest wave fitting the cavity is named the cut-off frequency f_c . For all frequencies lower than f_c the corresponding wavelengths do not fit inside the cavity and decay exponentially.

The discussed waves on a string are 1 dimensional waves, but the waveguide geometry of the pFEL is three dimensional, meaning waves must fit in three orientations. Waves fitting in the width and height of the waveguide are called transverse modes. Waves fitting along the length are called longitudinal modes. The waveguide is rectangular and the height and width are much smaller than its length. So the cut-off frequency is mostly determined by the transverse size. For more detail we review the wave equation for rectangular waveguides by using Maxwells equations.

3.3 TM modes in metallic rectangular waveguides

Maxwell's equations are the basis of electrodynamics. So analysing them will lead to the modes of the *empty* rectangular waveguide, including the phase velocity and field patterns. During derivation the well-known phasor notation is used to simplify analysis. An electric wave propagating in the z -direction is shown in eq. 3.1.

$$\mathbf{E} = \tilde{\mathbf{E}}(x, y, z)e^{j\omega t + \phi} \quad (3.1)$$

With \mathbf{E} the electric field, $\tilde{\mathbf{E}}$ a time independent amplitude of the oscillating field with the angular frequency ω , t time and ϕ a starting phase. It is customary to suppress the common phasor term $e^{j\omega t + \phi}$ in field equations to maintain readability. The starting phase is only shown when relevant.

Eq. 3.2 shows the source free Maxwell equations.

$$\nabla \times \mathbf{E} = \frac{-\partial \mathbf{B}}{\partial t} \quad (3.2a)$$

$$\nabla \times \mathbf{H} = \frac{\partial \mathbf{D}}{\partial t} \quad (3.2b)$$

$$\nabla \cdot \mathbf{D} = 0 \quad (3.2c)$$

$$\nabla \cdot \mathbf{B} = 0 \quad (3.2d)$$

As before \mathbf{E} is the electric field, as a function of the geometric variables x , y , z and time t . Using the same conventions: \mathbf{B} is the magnetic flux density field, \mathbf{H} the magnetic field and \mathbf{D} the electric flux density field.

Furthermore we will assume linear material properties and thus obtain the following relations for electric and magnetic flux density.

$$\mathbf{D} = \epsilon \mathbf{E} \quad (3.3a)$$

$$\mathbf{B} = \mu \mathbf{H} \quad (3.3b)$$

Where ϵ is the complex relative electrical permittivity and μ the complex relative magnetic permeability. Thus the Maxwell's eqs. 3.2a and 3.2b become

$$\nabla \times \mathbf{E} = -\mu \frac{\partial \mathbf{H}}{\partial t} \quad (3.4a)$$

$$\nabla \times \mathbf{H} = \epsilon \frac{\partial \mathbf{E}}{\partial t} \quad (3.4b)$$

Applying phasor notation to both equations leads to

$$\nabla \times \tilde{\mathbf{E}} = -j\omega\mu\tilde{\mathbf{H}} \quad (3.5a)$$

$$\nabla \times \tilde{\mathbf{H}} = j\omega\epsilon\tilde{\mathbf{E}} \quad (3.5b)$$

We take the curl of both sides of eq. 3.5a

$$\nabla \times \nabla \times \tilde{\mathbf{E}} = -j\omega\mu(\nabla \times \tilde{\mathbf{H}}) \quad (3.6)$$

And substituting $\nabla \times \tilde{\mathbf{H}}$ with eq. 3.5b.

$$\nabla \times \nabla \times \tilde{\mathbf{E}} = \omega^2\epsilon\mu\tilde{\mathbf{E}} \quad (3.7)$$

The resulting equation contains only the vector $\tilde{\mathbf{E}}$. This equation is simplified by using the vector calculus identity

$$\nabla \times \nabla \times \mathbf{X} = \nabla(\nabla \cdot \mathbf{X}) - \nabla^2 \mathbf{X} \quad (3.8)$$

allows eq.3.7 to be rewritten as

$$\nabla(\nabla \cdot \tilde{\mathbf{E}}) - \nabla^2 \tilde{\mathbf{E}} = \omega^2 \epsilon \mu \tilde{\mathbf{E}} \quad (3.9)$$

The metallic rectangular waveguide was assumed source free, $\nabla \cdot \mathbf{E} = 0$, resulting in the *Helmholtz equation*:

$$\nabla^2 \tilde{\mathbf{E}} + k^2 \tilde{\mathbf{E}} = 0 \quad (3.10)$$

Where $k = \omega \sqrt{\epsilon \mu}$ is the propagation constant or wavenumber of the medium.

Now we assume harmonic fields with a wave propagation along the z -axis. Let $\mathbf{e}(x, y) = e_x \cdot \hat{x} + e_y \cdot \hat{y}$ and $\mathbf{h}(x, y) = h_x \cdot \hat{x} + h_y \cdot \hat{y}$ be the transverse mode pattern for the electric and magnetic field respectively, where $e_z \cdot \hat{z}$ and $h_z \cdot \hat{z}$ are their respective longitudinal field components. Also assume the electric field actually has a non-zero z -component, as is required for bunching and gain. In this case the magnetic field is found in the transverse plane and the term $h_z \cdot \hat{z} = 0$ throughout the waveguide. The modes described here are called transverse magnetic modes (TM-modes) and are written as

$$\tilde{\mathbf{E}}(x, y, z) = [\mathbf{e}(x, y) + e_z(x, y)\hat{z}] e^{-j\beta z + \phi} \quad (3.11a)$$

$$\tilde{\mathbf{H}}(x, y, z) = [\mathbf{h}(x, y) + 0 \cdot \hat{z}] e^{-j\beta z + \phi} \quad (3.11b)$$

Here β is the constant of propagation. Reversing the sign of β changes the direction of propagation. Furthermore, a larger value corresponds to a shorter wavelength. β is governed by the geometry of the waveguide. ϕ is again a starting phase. Using this approach we can rewrite eqs. 3.5a and 3.5b to

$$\frac{\partial E_z}{\partial y} + j\beta E_y = -j\omega \mu H_x \quad (3.12a)$$

$$-\frac{\partial E_z}{\partial x} - j\beta E_x = -j\omega \mu H_y \quad (3.12b)$$

$$\frac{\partial E_y}{\partial x} - \frac{\partial E_x}{\partial y} = 0 \quad (3.12c)$$

$$j\beta H_y = j\omega \epsilon E_x \quad (3.13a)$$

$$-j\beta H_x = j\omega \epsilon E_y \quad (3.13b)$$

$$\frac{\partial H_y}{\partial x} - \frac{\partial H_x}{\partial y} = j\omega \epsilon E_z \quad (3.13c)$$

These six equations, (x, y, z for E and H), can be solved for the transverse

field components rewriting them in terms of E_z and H_z with $H_z = 0$:

$$H_x = \frac{j}{k_c^2} \left(\omega \epsilon \frac{\partial E_z}{\partial y} \right) \quad (3.14a)$$

$$H_y = \frac{-j}{k_c^2} \left(\omega \epsilon \frac{\partial E_z}{\partial x} \right) \quad (3.14b)$$

$$E_x = \frac{-j}{k_c^2} \left(\beta \frac{\partial E_z}{\partial x} \right) \quad (3.14c)$$

$$E_y = \frac{j}{k_c^2} \left(-\beta \frac{\partial E_z}{\partial y} \right) \quad (3.14d)$$

Where we introduced the cut-off wavenumber k_c defined as

$$k_c^2 = k^2 - \beta^2 \quad (3.15)$$

Equations eq. 3.14a to 3.14d are the solutions for TM-modes in a waveguide. They couple all field components to E_z meaning the Helmholtz equations need all to be solved for E_z . The other components are easily calculated from eqs. 3.14.

Next we demonstrate how to solve E_z for the TM-modes equations for source free rectangular metallic waveguides. The Helmholtz equation for E_z is written as:

$$\left(\frac{\partial^2}{\partial x^2} + \frac{\partial^2}{\partial y^2} + \frac{\partial^2}{\partial z^2} + k^2 \right) E_z = 0 \quad (3.16)$$

Recall eq. 3.11a, yielding $E_z(x, y, z) = e_z(x, y)e^{-j\beta z}$ allowing to rewrite the Helmholtz equation to a two dimensional variant

$$\left(\frac{\partial^2}{\partial x^2} + \frac{\partial^2}{\partial y^2} + k_c^2 \right) e_z(x, y) = 0 \quad (3.17)$$

Note the constant of propagation is substituted by the cut-off wavenumber using eq. 3.15, $k_c^2 = k^2 - \beta^2$. To solve eq. 3.17 the method of separation of variables is applied

$$e_z(x, y) = X(x)Y(y) \quad (3.18)$$

Thus equation yields

$$\frac{1}{X} \frac{d^2 X}{dx^2} + \frac{1}{Y} \frac{d^2 Y}{dy^2} + k_c^2 = 0 \quad (3.19)$$

Each term in eq. 3.19 must be equal a constant so we separate the cut-off wavenumber into two constants $k_x^2 + k_y^2 = k_c^2$ and can rewrite eq. 3.19 into

separate equations

$$\frac{d^2 X}{dx^2} + k_x^2 X = 0 \quad (3.20a)$$

$$\frac{d^2 Y}{dy^2} + k_y^2 Y = 0 \quad (3.20b)$$

These type of differential equations can be solved for $e_z(x, y)$. The general solution is

$$e_z(x, y) = (A \cos(k_x x) + B \sin(k_x x))(C \cos(k_y y) + D \sin(k_y y)) \quad (3.21)$$

The unknown constants can be found by determining the boundary conditions. Metals counteract any infringing electric field, thus the field at the surface must equal zero. Electric fields near a metal surface are parallel to the normal direction of that surface. In a rectangular metal waveguide all electric field vectors near surfaces lie in the transverse plane. For a metal waveguide of width a and height b , the following boundary conditions apply

$$e_z(x, y) = 0 \quad \text{at} \quad [x = 0, a, \quad y = 0, b.] \quad (3.22)$$

Applying the first boundary condition leads to $A = 0$ and $k_x = m\pi/a$ with m a positive integer. In a similar way, applying the second boundary condition shows $C = 0$ and $k_y = n\pi/a$ with n a positive integer.

The general solution now can be rewritten as a solution for E_z

$$E_z(x, y, z) = U_{mn} \sin \frac{m\pi x}{a} \sin \frac{n\pi y}{b} e^{-j\beta z} \quad (3.23)$$

where U_{mn} is an amplitude constant depending on the strength of the field.

With E_z solved, the TM_{mn} -mode wave equations, eqs. 3.14, from the previous section for all other components can be written down too

$$H_x = \frac{j\omega\epsilon n\pi}{bk_c^2} U_{mn} \sin \frac{m\pi x}{a} \cos \frac{n\pi y}{b} e^{-j\beta z} \quad (3.24a)$$

$$H_y = \frac{-j\omega\epsilon m\pi}{ak_c^2} U_{mn} \cos \frac{m\pi x}{a} \sin \frac{n\pi y}{b} e^{-j\beta z} \quad (3.24b)$$

$$E_x = \frac{-j\beta m\pi x}{ak_c^2} U_{mn} \cos \frac{m\pi x}{a} \sin \frac{n\pi y}{b} e^{-j\beta z} \quad (3.24c)$$

$$E_y = \frac{-j\beta n\pi y}{bk_c^2} U_{mn} \sin \frac{m\pi x}{a} \cos \frac{n\pi y}{b} e^{-j\beta z} \quad (3.24d)$$

Note that the wave equations are zero if either m or n is zero.

The phase velocity of a planewave propagating through a non-dispersive medium in open space is defined as $v_{ph} = \omega/k = 1/\sqrt{\mu\epsilon}$, which equals the

light velocity in the respective medium¹. The phase velocity of TM-mode waves in the waveguide are given by $v_{ph} = \omega/\beta$. Solving the propagation constant β

$$\beta = \sqrt{k^2 - k_c^2} = \sqrt{k^2 - \frac{m\pi^2}{a} - \frac{n\pi^2}{b}} \quad (3.25)$$

which is seen to be real, for propagating modes, when $k > k_c$. The cut-off frequency is given by

$$f_{c\ mn} = \frac{k_c}{2\pi\sqrt{\mu\epsilon}} = \frac{1}{2\pi\sqrt{\mu\epsilon}} \sqrt{\frac{m\pi^2}{a} - \frac{n\pi^2}{b}} \quad (3.26)$$

Eq. 3.25 shows $\beta < k$ which leads to

$$v_{ph} = \frac{\omega}{\beta} > \frac{\omega}{k} \quad (3.27)$$

the phase velocity of TM-waves in a waveguide is greater than light velocity c , see also fig. 2.7(a).

3.4 Wave propagation in a PhC

The PhC at hand for demonstrating the measurement technique is the one designed for the photonic free-electron laser under development at LPNO-UT. This particular PhC consists of a regular array of metal posts embedded in a rectangular waveguide. Wave propagation in an empty waveguide has been discussed in the previous section. Here we present how the PhC affects the wave propagation.

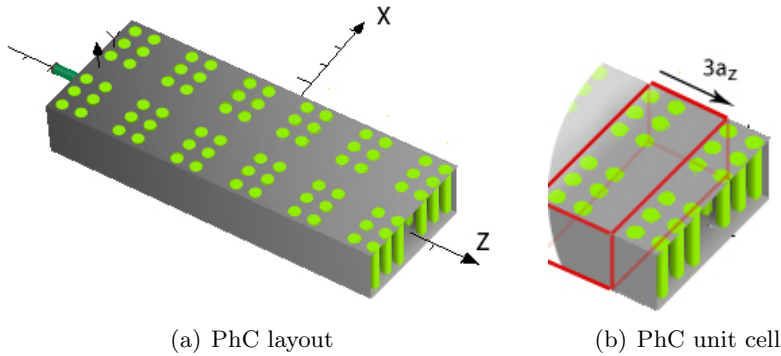


Figure 3.2: Photonic crystal slab

The PhC is schematically shown in fig 3.2 and designed to slow the

¹In a vacuum v_{ph} equals the light speed $c = 1/\sqrt{\mu_0\epsilon_0}$ with μ_0 and ϵ_0 the permeability and permittivity of vacuum respectively

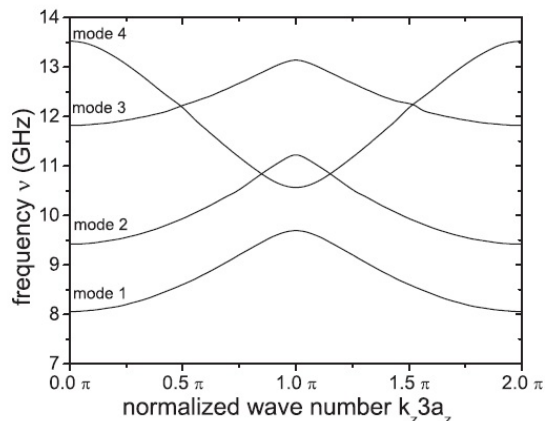


Figure 3.3: Calculated bandstructure

waves down to phase velocities $v_{ph} < 0.3c$ to match the available electron source. The embedded PhC supports modes with non-zero E_z field component, which are required for the pFEL. The PhC consists of a rectangular lattice of metal posts embedded in a rectangular waveguide. The width of the waveguide is $w = 47.25 \text{ mm}$ and height is $h = 20 \text{ mm}$. The cylindrical posts, depicted in green, have a diameter of $d = 4 \text{ mm}$. The spacing of the posts is $a_x = 6.75 \text{ mm}$ in the x -direction and $a_z = 7.5 \text{ mm}$ in the z -direction. The center posts along the z -axis have been removed to allow space for the electron beam to propagate and every third a_z a row of the lattice is missing. Thus the pattern repeats every $3a_z$, see fig. 3.2(b).

Wave propagation in a PhC waveguide is far more complex than a rectangular waveguide. Thus usually numerical calculation tools, like eigenmode solvers or FDTD methods, are used to retrieve dispersion and fields of PhC.

In this thesis a finite-difference time-domain (FDTD) numerical method [15] is applied to calculate the PhC waveguide modes. These types of calculations divide the structure into small mesh cells forming a 3D grid. The time-dependent Maxwell's equations are used to calculate the changes from grid to grid point using central-difference approximations. The resulting finite-difference equations are solved using leapfrog integration; First the electric field vectors at a given time and volume in space are calculated, then the magnetic field vectors are treated in the same volume at the next time step. This process repeats itself until a steady-state is reached.

Due to the periodicity of a PhC only the points in the first Brillouin zone, here $k = \left[0 \dots \frac{2\pi}{3a_z}\right]$, need to be calculated[12]. The results for the 4 lowest modes having a non-zero E_z -field component are shown in fig. 3.3. Note the dispersion is very different to the empty waveguides TM-modes. The PhC dispersion allows much lower phase velocities than the empty waveguide.

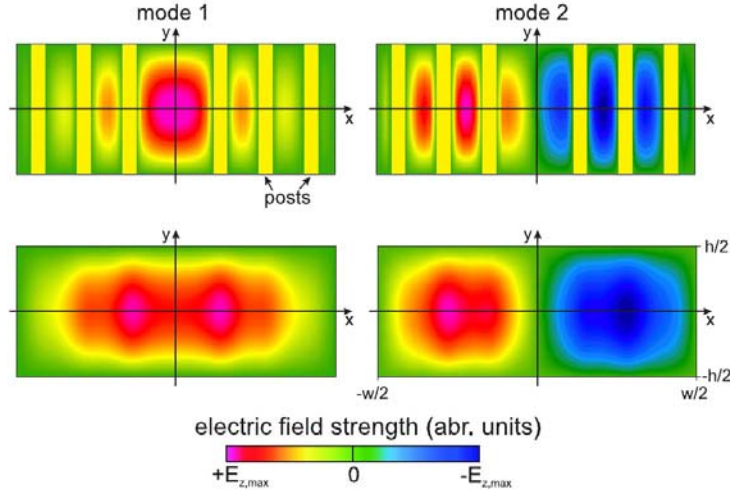


Figure 3.4: Calculated cross sections of the transverse E_z -mode patterns for mode 1 and mode 2 of the PhC at $z = 0.5a_z$ (upper fig.) and $z = 2.5a_z$ (lower) fig.

The 4th mode overlaps in frequency with other modes. This implies that at frequencies above 10.4 GHz multiple modes are expected to propagate at the same time. To prevent confusion the numbering is done where $k = 0$.

As noted earlier, the dispersion does not give any information on the electric field, but restricting the FDTD solver to solve a single frequency allows it to calculate the mode field patterns. Fig. 3.4 shows the E_z -field calculated for the first two modes at two positions within the unit cell. To achieve such a z -dependant field pattern the superposition of many so called spatial harmonics is required. The small range $k_z = \left[0 \dots \frac{2\pi}{3a_z}\right]$ is known as the first partial harmonic. Each following segment of the dispersion $k_z = \left[\frac{2\pi m}{3a_z} \dots \frac{(m+1)2\pi}{3a_z}\right]$ is called a higher spatial harmonic.

A single frequency of light thus propagates with multiple different wavenumbers and phase velocities at once in a PhC waveguide, however the field amplitude is usually mainly concentrated at the first partial harmonics [16].

3.5 Field distribution measurement

The method we apply is new to PhC, however, it is known for measuring fields in microwave resonators and we review the theory here [17].

The field is measured by observing the shift of resonant frequencies when a sub-wavelength object perturbs the fields. A simplistic way to visualise this is by representing the electromagnetic waves to be water waves of a river. The object would then be a wooden post sticking out of the water.

The waves propagating through the river reflect from and swirl around the wooden post. A great part of the water wave will move along unaffected by the small piece of wood. Further down the river the remainder of the wave has closed the wake behind the wooden post. Thus wave patterns do not change much if the object is small enough. But some of the water wave's momentum is stored or gained² in the swirl or around the object, meaning the frequency would change.

The resonant frequencies in a resonator change due to the same reason. A small amount of energy is stored around the perturbing object, affecting the resonant frequencies. The perturbed resonant frequency ω is given by

$$\omega^2 = \omega_0^2 \left(1 + \int (H_0(\mathbf{r})^2 - E_0(\mathbf{r})^2) dv \right) \quad (3.28)$$

where ω_0 is the unperturbed angular frequency of the cavity. The vector \mathbf{r} defines a spatial position in the PhC.

Assume the PhC is perturbed by an infinitesimal small object which sticks out of the waveguide wall. The integral in eq. 3.28 is taken over the perturbed volume. The fields H_0 and E_0 are normalized: $\int H(\mathbf{r})^2 dv = \int E_0(\mathbf{r})^2 dv = 1$ where the integration is over the whole unperturbed volume. Thus, when a perturbation is placed inside the PhC the fields at the point of the perturbation determine the frequency change which can be measured.

Which fields (H and/or E) or which field components ($E_z, E_x, E_y, H_z, H_x, H_y$) contribute to the frequency shifts depend on the material, shape, size and orientation of the object put in the PhC [11]. This allows to separately measure each field (components). For a simplification in the experiment a spherical metal bead is chosen. The bead perturbs both E and H fields as the metal used has $\epsilon \neq \epsilon_0$ and $\mu \neq \mu_0$ where ϵ_0 and μ_0 are the permeability and permittivity in vacuum. The bead selects no specific field component as a sphere has no preferred orientation.

To calculate the total frequency shift of a larger bead, an infinitely small bead is assumed at first. Thereby the field near the sphere reduces approximately to a static field, for which the solutions are easily calculated. The bead's size is then altered by an infinitesimal amount, and by integrating the change in frequency shift is retrieved. This process is repeated to grow the bead from 0 to its full dimensions.

The total frequency shift is then given by [17]

$$\frac{\omega_{r0}^2 - \omega_r^2}{\omega_{r0}^2} = 4\pi r^3 \left(E_0(\mathbf{r})^2 - \frac{1}{2} H_0(\mathbf{r})^2 \right) \quad (3.29)$$

²It is a bit of a stretch to visualise water waves gaining momentum from encounters with a wooden stick. This is the point where the example reached the limits of its analogy with EM-waves.

where ω_{r0}^2 is the unperturbed resonance frequency and ω_r^2 the perturbed resonance frequency. For very small frequency shifts $\Delta\omega_r = \omega_r - \omega_{r0} \ll \omega_{r0}$ the resonant frequency shift can be approximated by

$$\Delta\omega_r \cong 2\pi r^3 \left(-\frac{1}{2}H_0(\mathbf{r})^2 - E_0(\mathbf{r})^2 \right) \omega_{r0} \quad (3.30)$$

Recording $\Delta\omega_r$ as a function of the position \mathbf{r} in the PhC allows a detailed mapping of the field strength term $(-\frac{1}{2}H_0(\mathbf{r})^2 - E_0(\mathbf{r})^2)$. For the specific PhC used in the pFEL experiments all except E_z are zero at the waveguides center. Meaning, close to the center the measured shift in resonance frequency is proportional to E_z^2 which allows us to measure the E_z field component using a spherical bead. This is an important quantity as E_z is responsible for the bunching and hence the pFEL's gain.

Although this work uses the PhC of a pFEL to demonstrate the measurement technique, it is generally applicable to all types of PhC where the interior can be accessed to place a sub-wavelength object. This is not only true for PhC designed for microwave frequencies but the method can also be applied to all types of PhC, e.g., those designed to function using visible light, since these can be scaled to crystals functioning at microwave frequencies due to the scale invariances of Maxwell's laws for electrodynamics. This technique can therefore map the fields inside PhC and provide valuable information that is hard if not impossible to get otherwise.

Chapter 4

Experimental results

4.1 Introduction

Two experiments are designed to verify calculations and to investigate the experimental PhC. To identify the modes, whose fields are measured later, the dispersion of a PhC embedded in a metal waveguide is measured and compared to calculations. After identifying the modes its fields inside the PhC are measured. The measured field strength might deviate from the calculated values due to inevitable manufacturing disorder.

To maximize pFEL gain, electrons propagating through the pFEL's PhC should coincide with the maxima of the E_z field. The electron beam propagates through the structure's center. Measuring a field inside a PhC has never been done before, but we can apply a method previously only known for measuring microwave cavities.

The method relies on adding a perturbation inside a resonator. When measuring the resonant frequencies of the perturbed resonator a minute frequency shift is detected in the transmission and reflection spectra. The shape, size and material (susceptibility and permeability) of the object eventually determine which field components are scanned. This allows mapping of all components of the fields independently, or a combination of them, in the PhC.

4.2 Measurement of band structure

By computer calculation and measurements we first identify the different modes of the PhC.

The measurement relies on measuring cavity resonances of the PhC [12]. By restricting the light into a resonator we force it to fit into its geometry, meaning we know the wavelength inside the structure from the geometry¹.

¹This is only true if we are able to measure the longitudinal modes from the cut-off frequency and count each resonance.

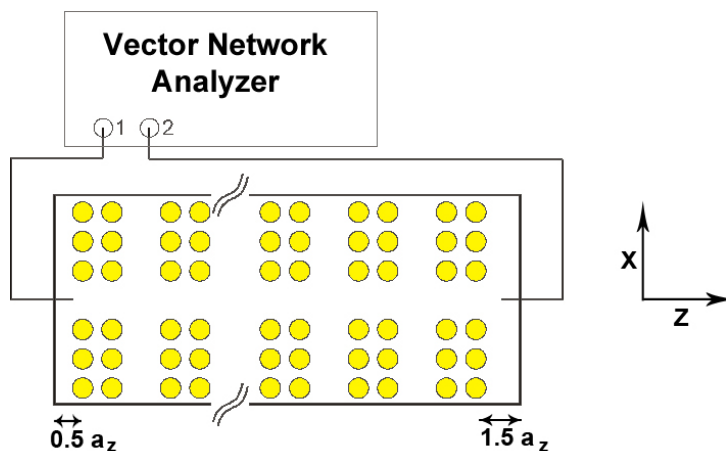


Figure 4.1: Dispersion measurement schematic

At certain frequencies ω_r the cavity is in resonance because the wavelength matches the resonator geometry exactly, which results in constructive interference between successive roundtrips.

In the experiment the PhC is placed between two mirrors to create this resonator. The transmission spectrum of this resonator is then measured by plotting the frequencies against the wavenumber, which is determined for the resonant geometry, we retrieve the dispersion $\omega(k)$

A resonator with an embedded periodic structure of N unit cells will exhibit $N+1$ discrete resonances[12]. These resonances have phase advances per unit cell that are equally spaced between 0 and π . The tested PhC is a slow wave structure of 15 periods (15 repetitions of the same pattern) and exhibits 16 discrete resonances. For each resonance a wave consisting of exactly ' r ' half wavelengths forms a standing wave along the z -axis of the PhC. The resonance with the lowest frequency will have $r = 1$, the second resonance $r = 2$, etc. and corresponds to the r -th longitudinal mode in the cavity.

In fig: 4.1 a schematic of the dispersion measurement setup is shown. Between two mirrors, 15 unit cells of the PhC are assembled. The left mirror is $0.5a_z$ away from the first row of posts and the right mirror $1.5a_z$. Thereby the total resonator length is exactly 15 unit cells. To allow in and out coupling of light into the resonator so called Hertzian dipole launcher/receivers are placed in the center of both mirrors, see fig.4.2(b). Both launcher and receiver are connected by coaxial cables to a scalar network analyser. This apparatus is able to measure transmission and reflection ratio's of light, required to determine the resonant frequencies of the PhC.

The PhC waveguide consists of two parts. The bottom part of the rectangular waveguide is milled out of a solid block of aluminium. The top is

closed by an aluminium plate. Both parts contain holes for mounting the posts. The brass posts have an inner diameter of $d = 2 \text{ mm}$ and an outer diameter of $d = 4 \text{ mm}$. The spacing of the posts is $a_x = 6.75 \text{ mm}$ in the x -direction and $a_z = 7.5 \text{ mm}$ in the z -direction. Screws extend from the top plate through the posts into the bottom plate fixating the posts into position. The total estimated positioning accuracy is $100 \mu\text{m}$ [18]. Two aluminium blocks are placed into the waveguide acting as highly reflective mirrors, creating the resonator. Through the center of the center of the mirrors the launcher sticks into the resonator as shown in fig. 4.2(b)

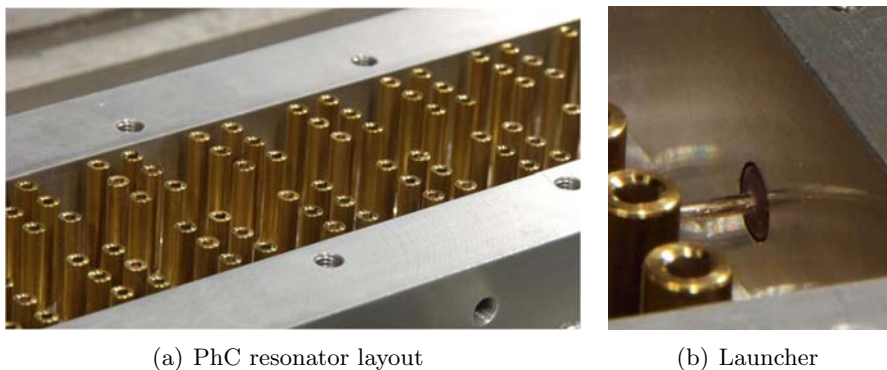


Figure 4.2: Resonator layout

A measured transmission from 7.9GHz to 12GHz is shown in fig.4.3(a). The lower frequency lies 0.1GHz below the cut-off frequency of the TM_{11} mode of the empty rectangular waveguide. The upper frequency lies on a level from where on multiple resonances are detected. At these frequencies multiple modes exist simultaneously. The pFEL's gain would be divided between the different modes. Therefore investigations focus on the single-mode region, 7.9 GHz to 9.8GHz where the highest gain is expected.

Below 8GHz, see fig. 4.3(a), the transmission is at the equipment's noise level -70dBm . This confirms there is no significant transmission below the TM-mode cut-off frequency of the waveguide. From the calculated dispersion fig. 3.3 we deduce the 15 peaks in region *A* are from the lowest order transverse mode, which has the lowest cut-off frequency. At around 10GHz, region *B*, the next mode is expected to appear, see fig. 3.3. However, the transmission is very low at this frequency ($< -50 \text{ dBm}$). The gap *B* in the center of fig. 4.3(a) is due to the mode pattern of mode 2. Recall from chapter 3, the second transverse mode has a node in the center of the waveguide. Both launcher and receiver are positioned at this node and are therefore incapable of exiting or receiving mode 2. After region *B* a few more peaks appear which we, using fig. 3.3, deduce to be of the 4th transverse mode before, at point *C*, the PhC becomes overmoded.

In fig. 4.3(b) the transmission of mode 1 is shown again, between 7.9

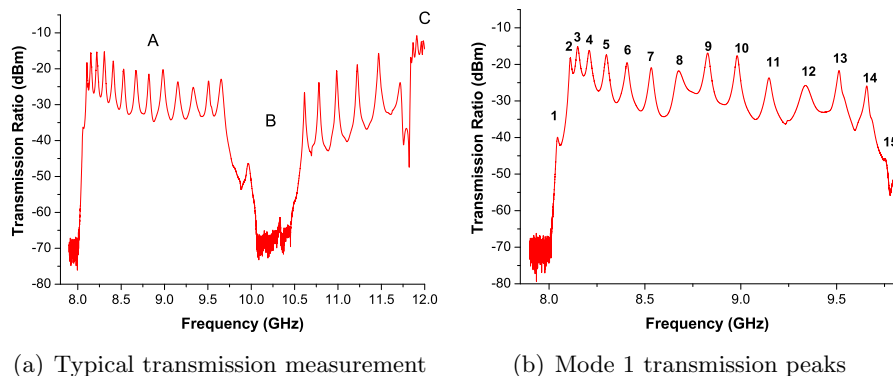


Figure 4.3: Transmission Readings

GHz and 9.7GHz. Each peak is numbered and belongs to a resonance for a longitudinal mode of mode 1. Resonance 1 corresponds to the mode pattern with the lowest wavenumber k_z and longest wavelength in the longitudinal direction. Resonance 15 has the highest wavenumber and shortest wavelength. According to H. Guo[12], theoretically 16 resonances should appear. The missing resonance, i.e. $k_z = 0$, is the resonance belonging to an infinite wavelength which is hardly excited by the short dipole launcher. Furthermore as its frequency is equal to the cut-off frequency it experiences huge losses inside the structure and is unable to propagate.

To compare the measured results with calculations, FDTD calculations are performed which consist of the PhC waveguide and both launchers. However, every metal post is assumed to be perfectly electrical conducting. Fig. 4.4(a) shows the calculation results.

The small deviations stem from simplification in the calculations where to a lossless waveguide is assumed. This means that differences in transmission and width of the peaks are to be expected but not in the position of the resonances. The width predicted by the simulation is not much smaller than experimentally observed and shows some noise. This is due to the limited calculation time and as the FDTD solution is not yet fully converged. For later comparisons this noise is removed using a peak position preserving FFT² filter[19].

Fig. 4.4(b) shows the comparison between measured transmission and the calculated transmission. As can be seen from the graph, calculated and measured peak positions are in very good agreement with each other, allowing to conclude area A contains resonances of the lowest order mode of the PhC and FDTD calculations are able to performance.

Finally, we determine the dispersion based on the measured peak positions. The total length of the waveguide is 15 periods of the PhC unitcell,

²See Appendix C at pag. 41 for more details

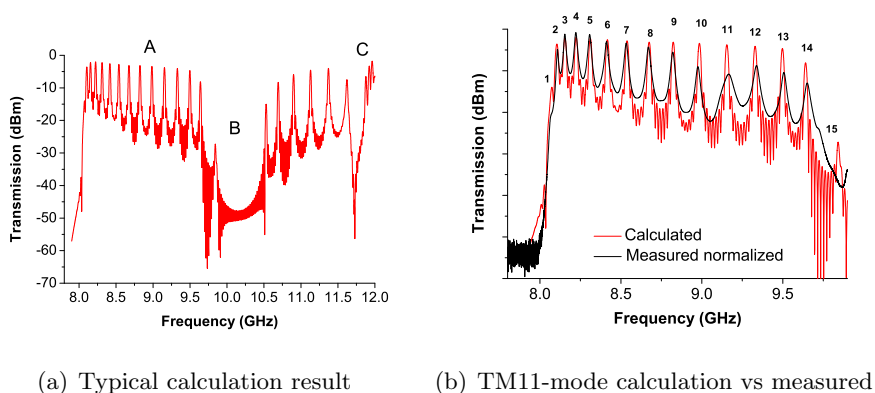


Figure 4.4: Calculated transmission

$L = 15 * 3 * a_z = 337.5$ mm. The 1st resonance (number 1 in fig. 4.3(a)) and 15th resonance cannot reliably be determined from the transmission due to their low coupling to the launcher. Dispersion is calculated using the remaining points.

The first resonance which is taken into account has frequency $f_2 = 8.1078$ GHz and wavenumber of

$$k_z = \frac{0.5r}{L} = 2.963m^{-1}$$

corresponding to a standing wave with 2 maxima and 3 nodes along the length of the waveguide. The remaining resonances are calculated³ in the same manner leading to fig. 4.5. A very good agreement is found again.

4.3 Field Characterization

In this section we present spatial mapping of field patterns inside a PhC waveguide. The goal is to map the lowest order transverse mode of the PhC waveguide to verify its E_z -field close to the waveguide center. This mode is crucial for pFEL operation because it possesses a strong electric field throughout the whole length of the waveguide. In order to bunch, i.e. produce coherent light, the electrons traveling through the center of the waveguide need to interact with the E_z field. Any deviations would lead to reduced gain.

To measure the fields we only add the perturbation object to the dispersion setup. The resulting setup is shown in fig. 4.6 The object perturbs each resonance frequency of the longitudinal modes. This is measured by observing the frequency shift of the transmissions peaks. As eq. 3.30 shows this

³For calculated values refer to the tables in Appendix B on pag. 39.

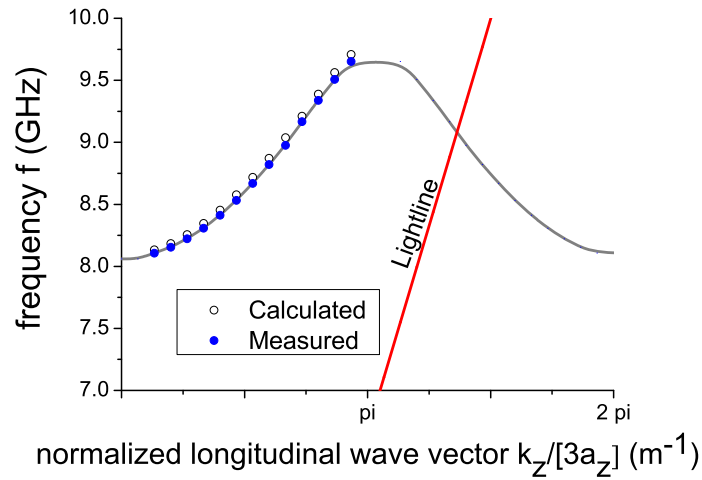


Figure 4.5: Comparison of measured and calculated band structure in the first spatial harmonic

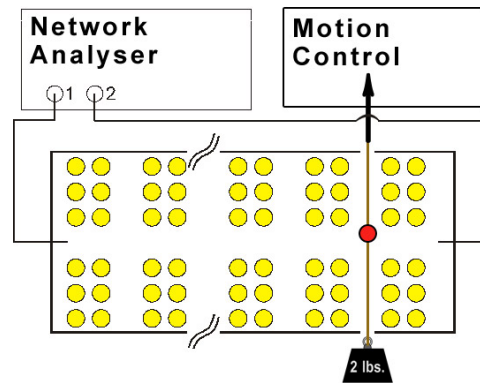


Figure 4.6: Schematic representation of a Field Characterization setup

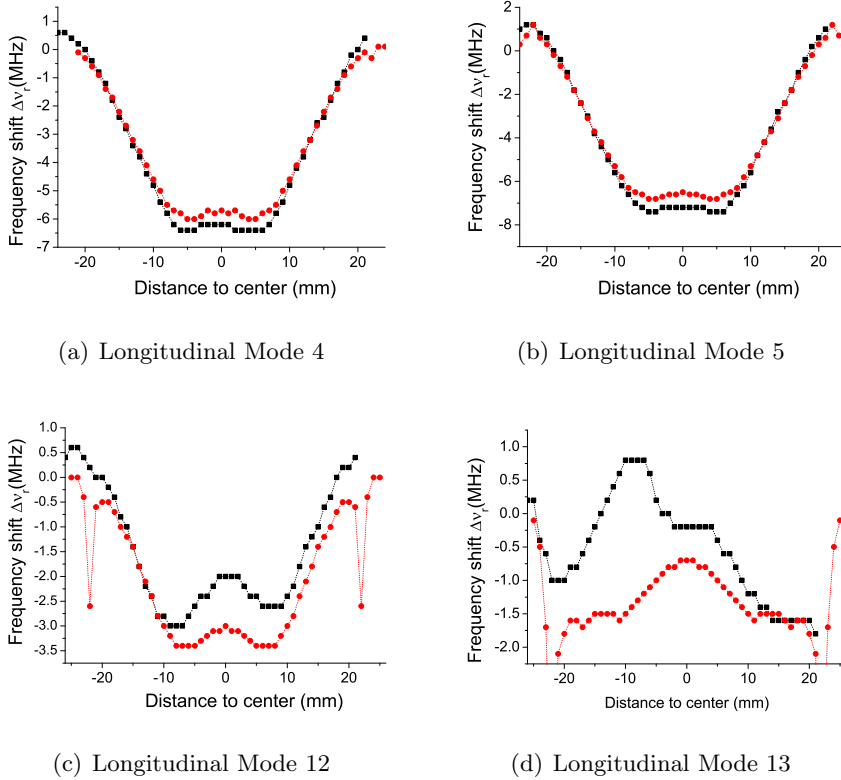


Figure 4.7: Frequency shifts for Transverse Mode 1

demonstrates the concept of the field map method. The object, a spherical bead, is mounted on a dielectric (nylon) string. This string is guided through the PhC by tiny holes in the waveguide wall. The string has a diameter of only 0.3mm and a low dielectric constant to have a minimum impact on the electromagnetic fields inside the PhC. At the end of the string, outside the PhC, a weight is attached to keep the string under constant tension. The other end of the string is mounted on a translation stage. By moving the translation stage the bead can be positioned with an accuracy of about 10 μm .

To confirm maximum field intensities in the center of the waveguide transverse slices of the waveguide are mapped along one missing row of a unit cell. Fig. 4.7 shows the shifts of resonances relative to the 3rd unit cell. The bead is moved by steps of 1mm, starting just outside the waveguide. At each position the measured resonance frequencies are normalized to the resonant frequencies with the PhC perturbed only by the nylon string to determine the relative frequency shifts due to the bead.

Fig. 4.7 shows the location of the bead relative to the center of the waveguide plotted against the measured resonance frequency shift. The

measured resonance frequency shifts (black squares) are compared to calculated resonance shifts (red dots) which were retrieved by using a FDTD method. Recall the resonance shift follows the sum of $(\frac{1}{2}H(r)^2 - E(r)^2)$. Negative shifts indicate dominant electric fields, while positive shifts indicate dominant magnetic fields.

In fig. 4.7(a) and 4.7(b) frequency shifts of longitudinal mode 4 and 5 are shown. The maximum frequency shift is -7.8 MHz, less than a 1/1000th of the resonant frequency in question. Both longitudinal modes reach quite a good agreement between measured and calculated results. The differences are likely due to the simplifications in the FDTD calculations.

Note right at the center the frequency shift is only due to the eigenmode pattern of the E_z field. This is because close to the center all other field components are nearly zero. Only further to the side walls do the other field components significantly contribute to the frequency shift. Therefore the measurement confirms that the electrons will experience a strong bunching force by the E_z field.

However higher modes (7–8 and 10–13) show bigger deviations to the calculations, see fig. 4.7(c) and 4.7(d). Due to PhC symmetry all modes considered should be symmetric around the zy-plane. As expected the calculations show symmetric shifts, but the measured frequency shifts show a clear asymmetry. We exclude misalignment of the string and the bead due to the high mechanical precision of all parts of the setup.

Thus the shown data seems to indicate a disorder of the PhC, due to e.g. an asymmetric post positioning. The disorder seems to be frequency dependant. A reason might be that lower longitudinal resonances have longer wavelengths than higher longitudinal resonances. In comparison to the positioning errors such modes are less sensitive to any disorder than higher modes. It is therefor expected that disorder has a higher impact for the higher longitudinal resonances.

Chapter 5

Conclusion

We have demonstrated a technique well known for measuring fields in microwave structures and applied it for the first time to successfully measure the internal field of a photonic crystal (PhC). The technique relies on placing the PhC in a microwave resonator and measure the resonant frequency shifts when a sub-wavelength object is placed in the PhC. The amount of frequency shift is related to the field strength at the objects position, thus allowing the fields to be mapped at any accessible part of the PhC. This has not been done before as the methods reported in literature only allow measurement outside the PhC itself.

The technique has been demonstrated by applying it to a PhC designed for use in a single beam photonic free electron laser (pFEL), which is a novel concept to produce laser light in the THz regime. The PhC has been characterized by measuring its band structure and a field measurement was performed, using a spherical metal bead, to map all fields and field components simultaneously. Results of both measurements are compared with FDTD calculations of the PhC.

The resonance measurements used to determine the band structure of the PhC where performed without the object present. The measured resonance frequencies are in good agreement with the calculated results.

With the sub-wavelength metal sphere present, we measured the frequency shift of the resonances and compared these with the calculated ones. Again for lower resonant frequencies belonging to longer wavelengths, a very good agreement was found. At higher resonant frequencies the the experimental results indicate asymmetries in the field that are not present in the calculations. This seems to indicate local disorder in the PhC that will manifest itself more clearly at smaller wavelengths.

The pFEL principle was reviewed in the theory and showed that a reduced phase velocity is requires for Cherenkov radiation emission. The radiation can only get coherent by bunching of the electron beam by the longitudinal electric field. The measurements and calculations indicate the

PhC fulfills both conditions and is thus suitable for use in a single beam pFEL.

The method presented here has successfully mapped the internal field in a PhC and is sufficiently sensitive to detect local disorders.

5.1 Recommendations

The applied method has further potential to investigate specific fields and field components. The orientation, shape and material (susceptibility and permeability) of the sub-wavelength object determine which fields or field components are perturbed, allowing them to be mapped separately.

The method is suitable to test any PhC due to the scale invariance of Maxwell's laws. I recommend making the rectangular metal waveguide suitable for easy replacement of the PhC with a structure of choice. Hereby other research groups might take interest in the setup to perform measurements in cooperation with LPNO-UT. This would benefit the group in both knowledge and relations.

Measurement speed can be improved by replacing the scalar network analyser for a more effective, but also very expensive, vector network analyser. Such an apparatus also provides phase information allowing for even more accurate resonance readings, improving sensitivity. A more cost effective solution could be the optimization of current equipment. The scalar network analyser and other equipment allow for continuous sweep measurements which are less accurate but much faster.

Appendix A

Phase and Group velocity of light

This appendix is attached as a quick refresher on the subject of phase and group velocities of light. The velocities are closely related and easily confused. We set out to discuss the correct interpretation via an example using a modulated wave.

A.1 Modulated Wave

The amplitude modulated wave is formed by superimposing two harmonic waves of angular frequency ω and wavelength λ where¹

$$\lambda_1 - \lambda_2 \neq \omega_1 - \omega_2 \quad \text{and} \quad \lambda_1 \neq \lambda_2$$

An example wave is shown in fig. A.1. The amplitude of a higher frequency wave is multiplied by the amplitude of a lower frequency wave, creating an amplitude envelope. The 6 pictures show chronological steps of a propagating example wave. The green dots indicate the positions of nodes created by the wave modulation. The red dot indicates a point of constant phase.

Phase velocity is expressed as the speed at which a point of constant phase propagates through space. In fig. A.1(a) a phase is chosen and denoted by the red dot on the left. The red dot tracks the location of this phase along the wave as time progresses through figures A.1(b), A.1(c), etc. The speed at which the red dot moves is the phase velocity.

The group velocity is often thought of as the speed at which energy or information is conveyed through a wave. It's given by the speed at which the amplitude envelope moves through space. The green dot tracks the node of the amplitude envelope along the wave. The speed at which the green

¹For extra clarity in the example a non-zero group velocity is selected by setting $\lambda_1 - \lambda_2 \neq \omega_1 - \omega_2$. To build a modulated wave this is not strictly necessary.

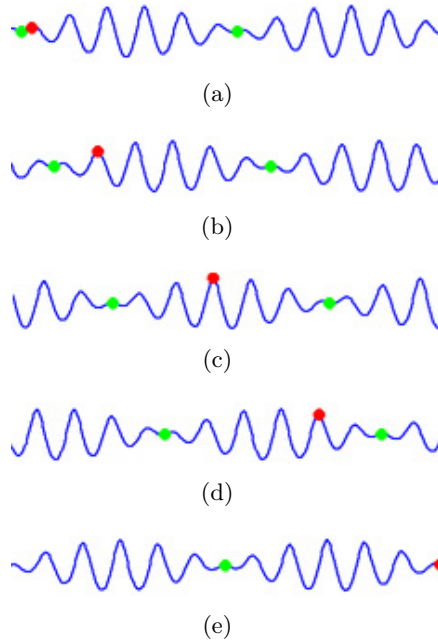


Figure A.1: Propagation of a modulated wave

dots move indicate the group velocity. The entirety of waves between two nodes is called a wavegroup.

As easily can be seen, the phase velocity in this example is higher than the group velocity. New waves seem to emerge at the back of the wavegroup, grow in amplitude until they are at the center of the wavegroup, and slowly disappear as they reach the front of the wavegroup. Group and phase velocities differ in dispersive media such as glass or in dispersive geometries such as waveguides. After a time $T/2$ the point of constant phase has traveled from one group node to the next, see fig. A.1(e).

A.2 Phase and group velocity relation

Phase and group velocity are related through (angular) frequency ω and wave vector \mathbf{k} as is shown in this section. Phase velocity v_{ph} can be written in relation to wavelength λ and period T using the fact that a 2π phase change has occurred when the crest of a wave has traveled a full wavelength. The point of constant phase must thus have traveled an equal distance in a time T as well.

$$v_{ph} = \frac{\lambda}{T}$$

Rewriting using $\mathbf{k} = 2\pi/\lambda \cdot \hat{z}$ with \hat{z} the propagation direction and $\omega = 2\pi/T$ gives phase velocity as function frequency ω and wave vector \mathbf{k} .

$$v_{ph} = \frac{\omega}{\mathbf{k}}$$

Group velocity is the velocity of the amplitude envelope. For two superimposed waves, wavegroups (amplitude envelopes) arise whenever the wavelengths differ. The wavegroups appear to travel when the frequencies of the waves differ. The ratio of frequency and wavelength differences determine the group velocity.

By use of the wavelength to wavevector relation, the wavelength is expressed as a difference in wavevector $\Delta\mathbf{k} = \mathbf{k}_1 - \mathbf{k}_2$. The difference in angular frequency is given by $\Delta\omega = \omega_1 - \omega_2$. For infinitesimal small differences and many superimposed waves the group velocity can be expressed as the derivative of the phase velocity!

$$c_{gr} = \frac{\delta\omega}{\delta\mathbf{k}}$$

Appendix B

Measured and Calculated resonance peaks

This appendix presents results of the dispersion measurement demonstrated on pag. 30. A comparison is found in table B.1 between calculated and measured resonance frequencies.

longitudinal mode	wavenumber (m^{-1})	ν_m (GHz)	ν_c (GHz)	Δ (MHz)
2	2.9630	8.1079	8.1343	26.4
3	4.4445	8.1537	8.184	30.3
4	5.9259	8.2216	8.2559	34.3
5	7.4074	8.3071	8.3457	38.6
6	8.8889	8.4113	8.4538	42.5
7	10.370	8.5331	8.5781	45.0
8	11.852	8.6702	8.7177	47.5
9	13.334	8.8205	8.871	50.5
10	14.815	8.9758	9.0363	60.5
11	16.296	9.1655	9.2104	44.9
12	17.778	9.3379	9.3891	51.2
13	19.259	9.5069	9.5624	55.5
14	20.741	9.651	9.7085	57.5

Table B.1: Measured resonant frequencies and corresponding wavenumbers

Here ν_m and ν_c are the measured and calculated frequency respectively, where $\Delta = \nu_c - \nu_m$.

Measured peak positions have an estimated accuracy of $\leq 500\text{kHz}$ depending on the stability of the mode. The estimated wavelength accuracy is $\pm 200\mu\text{m}$ [18].

Appendix C

FFT Smoothing

This appendix illustrates the effect of FFT smoothing on repeatability of the dispersion measurement. Two consecutive dispersion measurements are performed as demonstrated in section 4.2. The measurements are identical and performed by the same operator. Variations in measured transmission would indicate a low repeatability and a high uncertainty in the dispersion results. The test result here is meant to be indicative not conclusive. Gathering statistically significant amounts of data costs excessive amounts of time while not a top priority for our research.

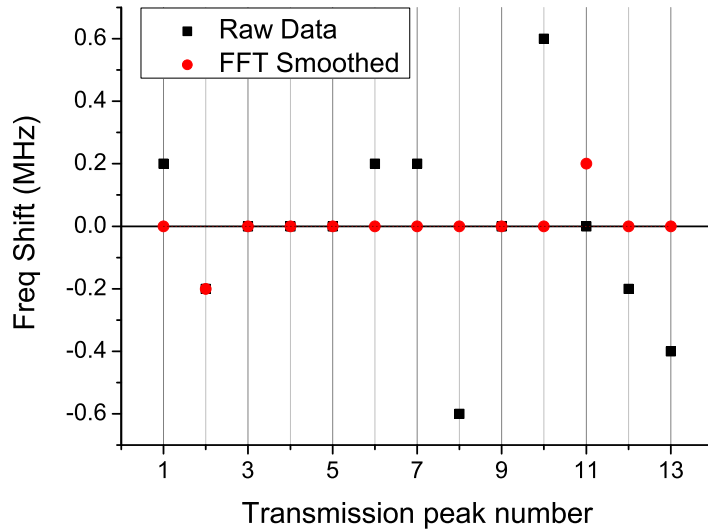


Figure C.1: Peak frequency detection variation in 2 consecutive PhC dispersion measurements

The variation in measured transmission peak positions of the disper-

sion measurement is shown in fig. C.1. The frequency resolution is set to 200kHz. The black and red points show the frequency difference of 13 measured transmission maxima. The black points indicate differences for each transmission maxima as determined from the raw data. The red points indicates the frequency differences between two measurements after applying FFT smoothing [19] at the data. The FFT smoothing removes quick variations, such as noise, from the data stream while conserving the general peak position. The results indicate that FFT smoothing could enhance repeatability significantly.

Bibliography

- [1] T. Baba, “Slow light in photonic crystals,” *Nat. Phot.* **2**, 465 (2008).
- [2] J. D. Joannopoulos, S. G. Johnson, J. N. Winn, and R. D. Meade, *Photonic Crystals Molding the flow of light* (Princeton University Press, 2008).
- [3] Yablonovitch and et al., “Inhibited Spontaneous Emission in Solid-State Physics and Electronics,” *Phys. Rev. Lett.* **58**, 2059 (1987).
- [4] Yi and et al., *App. Phys. Lett.* **81**, 4112 (2002).
- [5] Y. Akahane, *Nature* **425**, 944 (2003).
- [6] B. M. Cowan, *Phys. Rev.*, STAB **11**, 011 301 (2008).
- [7] E. Jerby, “Traveling-wave free-electron laser,” *Phys. Rev. A* **44**, 703–715 (1991).
- [8] P. J. M. van der Slot, “The photonic FEL: Toward a handheld THz FEL,” *FEL2008, Gyeongju* **2**, 231 (2008).
- [9] K. Okamoto, M. Loncar, T. Yoshie, and A. Scherer, “Near-field scanning optical microscopy of photonic crystal nanocavities,” *Appl. Phys. Lett.* **82**, 1676–1678 (2003).
- [10] M. Woldeyohannes, J. O. Schenk, R. P. Ingel, S. P. Rigdon, M. Pate, J. D. Graham, M. Clare, W. Yang, and M. A. Fiddy, “Internal field distribution measurement in 1-D strongly anisotropic sub-wavelength periodic structures of finite length,” *Opt. Expr.* **19**, 81–92 (2011).
- [11] J. C. Slater, “*Microwave Electronics*,” Van Nostrand, New York (1950).
- [12] H. Guo, Y. Carmel, W. R. Lou, L. Chen, J. Rodgers, D. K. Abe, A. Bromborsky, W. Destler, and V. Granatstein, “A Novel Highly Accurate Synthetic Technique for Determination of the Dispersive Characteristics in Periodic Slow Wave Circuits,” *IEEE Trans. Microwave Theory Tech.* **40**, 2086–2094 (1992).

- [13] E. Hecht and A. Zajac, *Hecht: Optics* (2003).
- [14] J. D. Jackson, *Classical Electrodynamics, 3rd edition* (Wiley, 1998).
- [15] “Concerto V7.0 Vectorfields LTD.” .
- [16] M. R. Amin, K. Ogura, T. Kobayashi, Y. Suzuki, and T. Watanabe, “Electromagnetic Field Properties of Axial Modes in a Finite Length X-Band Slow Wave Structure,” *J. Phys. Soc. Jap.* **65**, 627–634 (1995).
- [17] L. C. Maier and J. C. Slater, “Field Strength Measurements in Resonant Cavities,” *J. Appl. Phys.* **23**, 68 (1952).
- [18] G. J. M. Oude Meijers, “Personal communication,” .
- [19] “Origin SR 7.0 Originlab Corporation,” (2002).